International Journal of Plasticity 27 (2011) 868–886

Contents lists available at ScienceDirect

International Journal of Plasticity

journal homepage: www.elsevier.com/locate/ijplas

Rate dependent finite strain constitutive model of polyurea

Jongmin Shim [a], Dirk Mohr [a,b,*]

[a] Impact and Crashworthiness Laboratory, Department of Mechanical Engineering, Massachusetts Institute of Technology, Cambridge, MA, USA
[b] Solid Mechanics Laboratory (CNRS-UMR 7649), Department of Mechanics, École Polytechnique, Palaiseau, France

ARTICLE INFO

Article history:
Received 7 October 2009
Received in final revised form 7 October 2010
Available online 16 October 2010

Keywords:
Constitutive modeling
Polyurea
Nonlinear viscoelasticity
Finite strains

ABSTRACT

Continuous loading and unloading experiments are performed at different strain rates to characterize the large deformation behavior of polyurea under compressive loading. In addition, uniaxial compression tests are carried out with multistep strain history profiles. The analysis of the experimental data shows that the concept of equilibrium path may not be applied to polyurea. This finding implies that viscoelastic constitutive models of the Zener type are no suitable for the modeling of the rate dependent behavior of polyurea. A new constitutive model is developed based on a rheological model composed of two Maxwell elements. The soft rubbery response is represented by a Gent spring while nonlinear viscous evolution equations are proposed to describe the time-dependent material response. The eight material model parameters are identified for polyurea and used to predict the experimentally-measured stress–strain curves for various loading and unloading histories. The model provides a good prediction of the response under monotonic loading over wide range of strain rates, while it overestimates the stiffness during unloading. Furthermore, the model predictions of the material relaxation and viscous dissipation during a loading–unloading cycle agree well with the experiments.

1. Introduction

Polyurea is used to mitigate structural damage during impact loading because of its good damping performance. In addition, it is utilized by various industries because of its fast setting time as well as its good chemical and fire resistance. It has found applications in army vehicles for blast protection because of its high toughness-to-density ratio at high strain rates. Several researchers reported that polyurea shows a highly nonlinear viscoelastic behavior at finite strains (e.g. Amirkhizi et al., 2006; Bogoslovov and Roland, 2007; Roland et al., 2007; Shim and Mohr, 2009). The mechanical properties of linearly viscoelastic materials may be described by the relaxation modulus (or creep compliance) which is independent of strain magnitude. However, nonlinear viscoelasticity is characterized by a decrease (or increase) of the relaxation modulus (or creep compliance) with increasing strain or decreasing stress (e.g. Brinson and Brinson, 2008).

Most finite viscoelasticity models of elastomers are formulated using either (1) the so-called hereditary integral approach or (2) the framework of multiplicative decomposition of the deformation gradient. Motivated by linear viscoelastic models, hereditary integral models are formulated in terms of relaxation or memory functions (e.g. Lockett, 1972). Widely used single integral theories are the theory of Finite Linear Viscoelasticity (Coleman and Noll, 1961) and the Bernstein, Kersley and Zaps (BKZ) Theory (Bernstein et al., 1963); both make use of several relaxation/memory functions. Significant efforts have been made to improve these theories and to reduce the number of required material parameters (e.g. Lianis, 1963; McGuirt and Lianis, 1970; Leonov, 1976; Johnson et al., 1994; Haupt and Lion, 2002). Nonlinear viscoelastic behavior is often considered as the superposition of a rate-independent nonlinear elastic response (so-called equilibrium part) and a

---

* Corresponding author at: Solid Mechanics Laboratory (CNRS-UMR 7649), Department of Mechanics, École Polytechnique, Palaiseau, France.
E-mail address: mohr@lms.polytechnique.fr (D. Mohr).

0749-6419/$ - see front matter © 2010 Elsevier Ltd. All rights reserved.
doi:10.1016/j.ijplas.2010.10.001

viscosity-induced overstress contribution which is described through fading memory functions (e.g., Krempl et al., 1984). Most nonlinear viscoelastic constitutive models have been experimentally validated at very low strain-rates of 0.1/s or less. Only few papers deal with the nonlinear viscoelastic behavior of elastomers at intermediate and high strain-rates (1–1000/s). Using the hereditary integral approach, Yang et al. (2000) and Shim et al. (2004) proposed a phenomenological constitutive model to predict the behavior of silicon rubber at high strain rates (900–3000/s). Hoo Fatt and Ouyang (2007) adopted the integral approach to model the response of butadiene rubber at strain rate ranging from 76/s to 450/s. The validity of most hereditary integral approach based models is limited to a narrow range of strain rates due to the use of only one relaxation time period (Yang et al., 2000; Shim et al., 2004) or a constant memory function (Hoo Fatt and Ouyang, 2007). In general, the hereditary integral approach is very useful in describing finite viscoelastic behavior, but its successful application to the real test data depends strongly on the effectiveness of the rather complex relaxation or memory function calibration procedures.

Compared to hereditary integral models, the multiplicative decomposition of the deformation gradient typically leads to models with material parameters that can be easily identified from experiments. The concept of the multiplicative decomposition of the deformation gradient (Kröner, 1960; Lee, 1969) was initially applied to finite viscoelasticity by Sidoroff (1974) and further explored by others (e.g. Lubliner, 1985; Le Tallec et al., 1993; Reese and Govindjee, 1998; Huber and Tsakmakis, 2000). To model the viscoelastic behavior of elastomeric materials, Lion (1997a,b) has also applied the concept of multiplicative viscoelasticity in combination with nonlinear viscosity functions. The nonlinear viscoelasticity is commonly described through a rheological spring-dashpot model that features a rate-independent equilibrium part and a rate-dependent viscous part. In particular, Zener models are widely used (e.g. Roland, 1989; Johnson et al., 1995; Bergström and Boyce, 1998; Huber and Tsakmakis, 2000; Quintavalla and Johnson, 2004; Bergström and Hilbert, 2005; Qi and Boyce, 2005; Tomita et al., 2008; Areias and Matous, 2008). Zener models are composed of a spring (rate-independent part) in parallel with a Maxwell element (rate-dependent part). The constitutive model of the time-dependent part includes an evolution equation for the viscous deformation. The simplest evolution equation is a linear viscous flow rule (e.g. Amin et al., 2002; Johlitz et al., 2007). However, experiments have shown that the viscosity at finite strains is a function of the driving stress (e.g. Amin et al., 2006), the strain (e.g. Amin et al., 2006; Hoo Fatt and Ouyang, 2008) and/or the strain-rate (e.g. Khan et al., 2006). Thus, nonlinear viscous flows rules have been developed using a micro-mechanism inspired approach (e.g. Bergström and Boyce, 1998; Palm et al., 2006) or a purely phenomenological approach (e.g. Khan and Zhang, 2001; Colak, 2005; Amin et al., 2006; Khan et al., 2006; Hoo Fatt and Ouyang, 2008).

In order to represent the equilibrium contribution as the nonlinear elastic spring, rubber elasticity models are employed using the conventional material types such as neo-Hookean (e.g. Johlitz et al., 2007), Mooney–Rivlin, (e.g. Huber and Tsakmakis, 2000), or Arruda and Boyce's (1993) eight-chain model (e.g. Bergström and Boyce, 1998; Tomita et al., 2008). Other research groups (e.g. Amin et al., 2002, 2006; Hoo Fatt and Ouyang, 2008) used modified conventional material models to describe the high initial stiffness and the subsequent strain hardening.

Although several researcher have recently reported on experimental behavior of various polymeric materials for a wide range of strain rates (e.g. Khan and Farrokh, 2006; Mulliken and Boyce, 2006; Sarva et al., 2007), very little research has been reported on the modeling of elastomeric materials for loading and unloading for a wide range of strain rates. As for the hereditary integral approach based models, most multiplicative decomposition based models have been experimentally validated for a narrow range of strain rates. Quintavalla and Johnson (2004) adopted the Bergström–Boyce model to describe the dynamic behavior of cis-(1, 4) polybutadiene at high strain-rate of 3000–5000/s. Recently, Hoo Fatt and Ouyang (2008) proposed a thermodynamically consistent constitutive model with modified neo-Hookean rubber elastic springs to describe the steep initial stiffness of virgin butadiene rubber under tensile and compressive loading at intermediate strain rates (76–450/s). Dusunceli and Colak (2008) modified the viscoplasticity theory based on overstress (VBO) to account for the influences of crystallinity ratio on loading–unloading, creep and relaxation behaviors of semicrystalline polymers. Ayoub et al. (2010) suggested a model composed of a visco-hyperelastic network resistance in parallel with a viscoelastic–viscoplastic intermolecular resistance to describe the monotonic loading and unloading behavior of high density polyethylene.

The present work focuses on the modeling of the loading and unloading response of polyurea over a wide range of strain rates (from 10^{-3}/s to 10^{1}/s) and at large compressive strains (up to 1.0). Using the framework of the multiplicative decomposition of the deformation gradient, the rheological concept of two parallel Maxwell elements is employed to develop a nonlinear viscoelastic finite strain constitutive model. Guided by similar developments in area of rate-dependent plasticity models for glassy polymers (e.g. Qi and Boyce, 2005; Anand and Ames, 2006; Anand et al., 2009; Ames et al., 2009), the high stiffness of elastomers at small deformations is modeled using Hencky's strain energy function. In view of the simulation of blast and impact events, we limit our attention to the mechanical behavior of polyurea in its virgin state. After presenting all experimental results in Section 2, the constitutive model is detailed in Sections 3 and 4. A discussion of the comparison of simulations and experimental results for polyurea is given in Section 5.

2. Experimental investigation

2.1. Material

The polyurea specimens used in the study are extracted from a 12.7 mm thick polyurea DragonShield-HT Explosive Resistant Coating (ERC) layer on a steel armor plate. After separation from the plates, the polyurea specimens of diameter

D_0 = 10 mm and length L_0 = 10 mm are machined using conventional milling procedures. The shelf life of the polyurea prior to testing was about 4 years. All experiments are performed on polyurea in its virgin state (condition after curing. no prior mechanical loading history).

2.2. Relaxation experiments

The nonlinearity of the viscoelastic behavior of polyurea at low and intermediate strain rates is identified from relaxation tests. Using a hydraulic universal testing machine (Model 8800, Instron), the material is rapidly loaded to a prescribed strain level at the beginning of the experiment. The strain is subsequently kept constant while stress relaxation takes place. Nine relaxation tests are performed for true compressive strains ranging from $\varepsilon_0 = -0.048$ to -1.0. The engineering strain rate during the rapid loading phase was about 0.5/s. In order to capture the short-term viscoelastic behavior, the sampling frequency of the data was 5 kHz; the stress is recorded for about 10 min to identify the long-term behavior. Fig. 1a shows the recorded stress histories for various constant strain loadings. While the test duration was not long enough to observe the asymptotic long-term behavior (i.e. equilibrium modulus), the results indicate that the sampling frequency of 5 kHz is high enough to capture the asymptotic short-term viscoelastic behavior (i.e. initial relaxation modulus).

The relaxation moduli are computed using the definition

$$H(t) = \frac{\sigma(t)}{\varepsilon_0}, \tag{1}$$

where $\sigma(t)$ is the time history of the measured true stress for a constant strain of ε_0 (Fig. 1a). The corresponding relaxation modulus histories (Fig. 1c) clearly demonstrate the nonlinear viscoelastic nature of the material response: the relaxation modulus decreases from 120 MPa (at the strain of -0.048) to 20 MPa (at the strain of -1.0) at the beginning of relaxation; after more than 10 minutes, the corresponding relaxation moduli are 60 MPa and 10 MPa, respectively. The strong nonlinear nature of the viscoelastic behavior becomes also apparent when plotting the isochronous stress–strain curves (Fig. 1e).

2.3. Continuous compression experiments

In addition to relaxation experiments, constant strain rate loading and unloading tests are performed at absolute true strain rates between 10^{-3}/s and 10^{1}/s (Fig. 2a). The measured true stress versus logarithmic strain curves for five different strain rates are summarized in Fig. 2b. At least two tests are performed at each strain rate to confirm the repeatability of the experimental results. During the loading phase, the observed stress level exhibits strong strain rate sensitivity. For example, the observed stress level for 10^{-3}/s is about twice as high as for 10^{1}/s. However, during unloading, all the stress–strain curves seem to converge to the same curve regardless of the unloading strain rate.

2.4. Multistep compression experiments

In order to investigate the stress relaxation behavior during loading and unloading, experiments are performed with multistep strain history profiles. Similar experiments have been employed by other researchers (e.g. Lion, 1996; Bergstrom and Boyce, 1998; Qi and Boyce, 2005). Fig. 3a shows the applied strain history as a function of the normalized time $t|\dot{\varepsilon}/\varepsilon_0|$. The same maximum strain of $\varepsilon_0 = -1.0$ is chosen for all experiments. Experiments are performed for $|\dot{\varepsilon}| = 10^{-3}/\text{s}, 10^{-2}/\text{s}, 10^{-1}/\text{s}, 10^{0}/\text{s}$ and $10^{1}/\text{s}$; each experiment involves eight segments of constant strain and the corresponding durations of the hold times at constant strain are 1000, 100, 10, 1, 0.1 s, respectively. All measured stress–strain curves are depicted in Fig. 3b. The results from the multistep compression tests confirm the previous observation of high strain rate sensitivity during loading phase along with nearly rate independent behavior during unloading. Also the magnitude of stress relaxation during the loading phase is found to be larger than that during unlading. The superposition of the results from the monotonic and multistep compression experiments (Fig. 3d) shows that the specimens recover the virgin state resistance (described by the curves from the monotonic tests) after each relaxation period in the multistep compression experiment. The resistance recovery appears to be slower for large strains and high strain rates.

3. Constitutive model

3.1. Motivation

In the framework of multiplicative decomposition of the deformation gradient, models of the Zener type (Maxwell element in parallel with a spring) are widely used since these can effectively represent the nonlinear viscoelastic behaviors of many elastomers. For Zener models, it is common practice to identify the equilibrium path (the expected rate independent part of the stress–strain response) and the overstress contribution from the experimental stress–strain curves. The equilibrium path corresponds to the average stress–strain curve which can be determined in an approximate manner from two alternative approaches: (1) taking the mid-path of stress–strain curves from the monotonic loading and unloading test (e.g. Bergstrom and Boyce, 1998); (2) connecting the stress relaxation mid-points between loading and unloading phase from

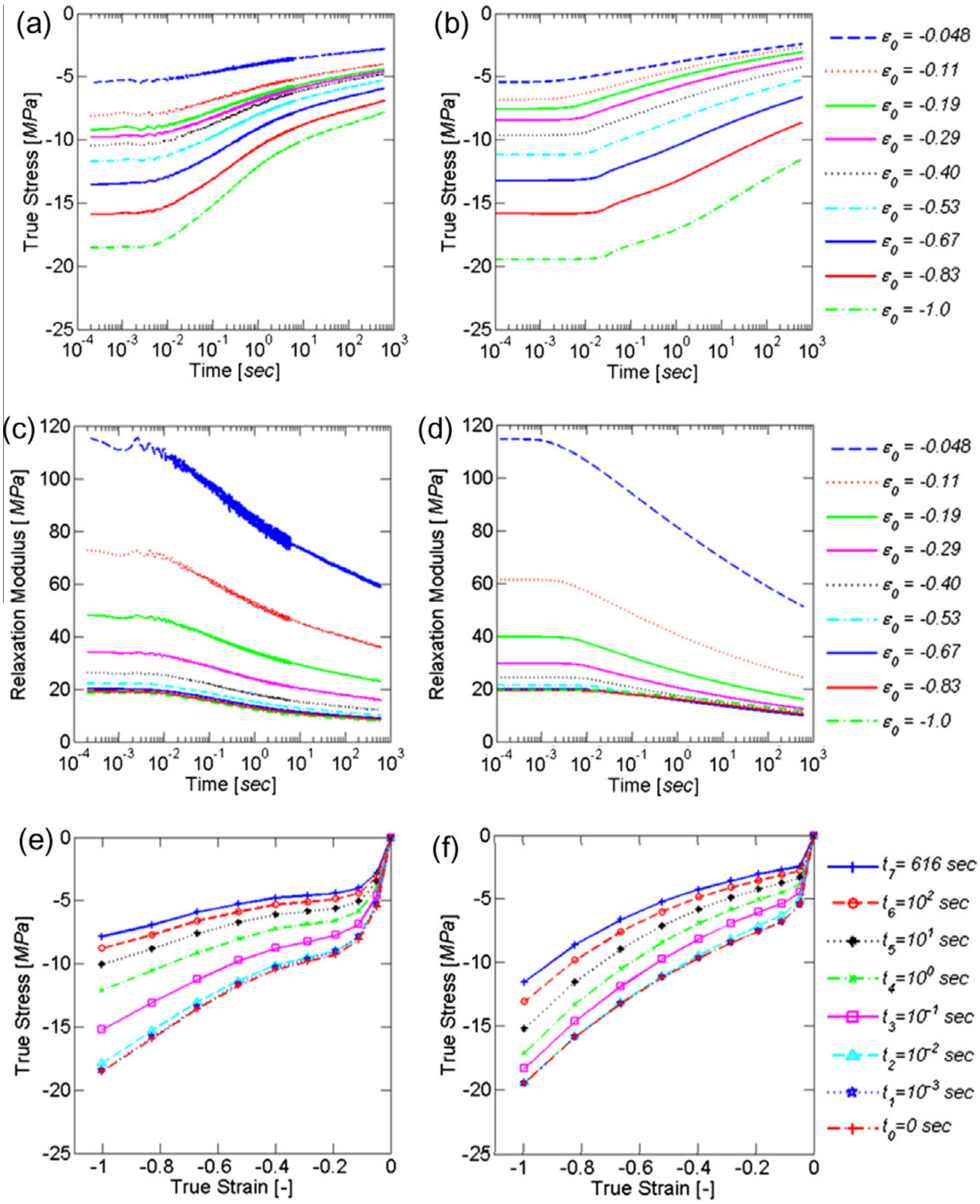

Fig. 1. Results of relaxation tests (left column) and corresponding simulations (right column). (a, b) True stress histories, (c, d) relaxation moduli histories and (e, f) isochronous stress–strain curves for different instants after the rapid strain loading.

the multistep compression tests (e.g. Qi and Boyce, 2005). Fig. 4 shows the average stress–strain curves as identified from the continuous compression tests at different strain rates. The summary plot in Fig. 6a clearly shows that the indentified average stress–strain curves depend on the strain rate. For instance, at a strain of −1.0, an average stress of −10 MPa is found from the experiment at 10^{-3}/s while an average stress of −17 MPa is obtained from the experiment at 10^{1}/s. This important observation is confirmed by the multistep compression tests. Recall from Fig. 3b that the amount of stress relaxation is different for loading and unloading. Thus, it is concluded that the concept of equilibrium path breaks down in the case of polyurea. Consequently, rheological models of the Zener type will not be able to describe the nonlinear viscoelastic behavior of polyurea for both loading and unloading.

Thermoplastic polyurethanes exhibit a two-phase structure composed of aliphatic soft segments and aromatic hard segments which is due to combining polyamine with isocyanate (e.g., Samson et al., 1997; Fragiadakisa et al., 2010). These segments are incompatible which results in the formation of soft and hard domains. In models of the Zener type, the rate

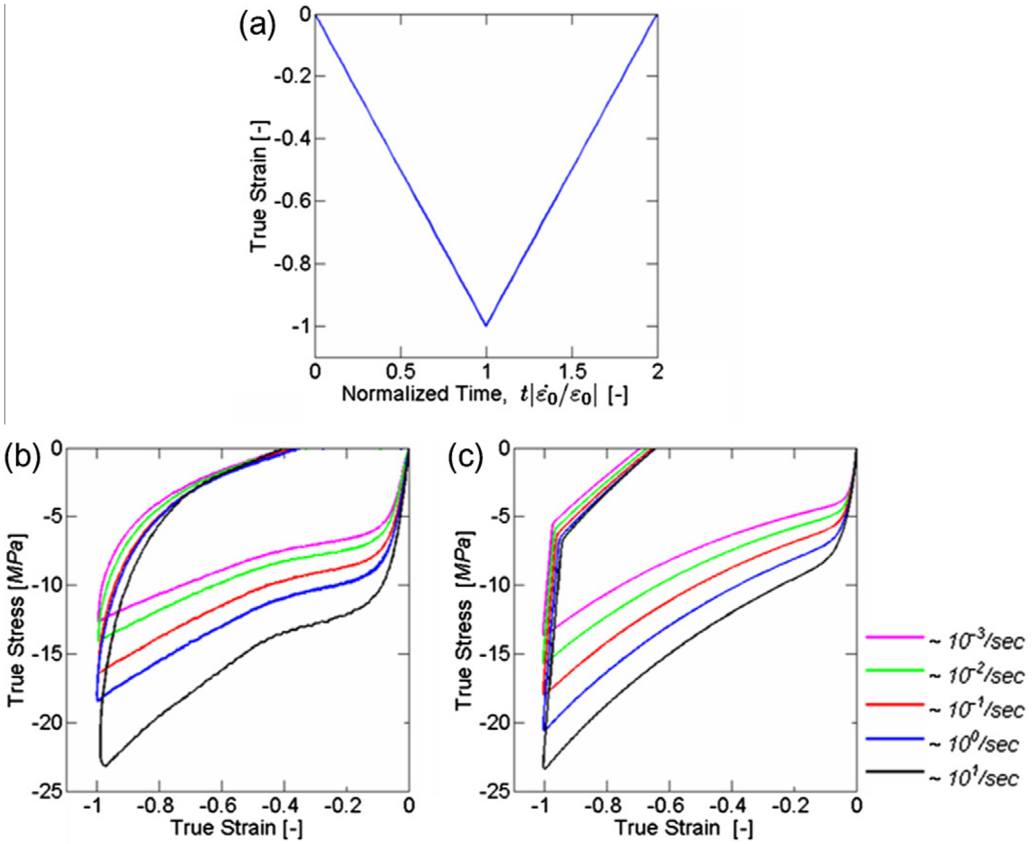

Fig. 2. Results of continuous loading/unloading experiments and corresponding simulations. (a) History of applied strain. Note that time in the *x*-axis is normalized by the total testing duration $|\varepsilon_0/\dot{\varepsilon}_0|$ where $\varepsilon_0 = 1$ and $\dot{\varepsilon}_0 = 10^{-3},\ 10^{-2},\ 10^{-1},\ 10^{0}$ and 10^{1}/s. (b) Stress–strain curves obtained from experiments and (c) corresponding simulations.

independent part is represented by a spring element. Qi and Boyce (2005) explained in their paper on the micro-mechanism inspired constitutive modeling of thermoplastic polyurethanes in which the spring element represents the entropic resistance of the soft domains in polyurethanes, while the rate dependent behavior of the hard part is represented by the Maxwell element of the Zener model. Due to the apparent rate dependency of the calculated average stress–strain curves, we substitute the spring of the Zener model by another Maxwell element. The resulting rheological model, two Maxwell springs in parallel (Fig. 5), has already been considered in the past by Boyce et al. (2000) and Dupaix and Boyce (2007) to describe the finite strain behavior of amorphous polymers. In the context of amorphous polymers near glass transition temperature, two Maxwell elements have been used to represent the rate-dependent inter- and intra-molecular network resistances under monotonic loading conditions.

In the following, we outline the constitutive equations for each of the four basic elements of our rheological model. Throughout our presentation, we refer to the Maxwell element that is predominantly associated with the deformation resistance of the soft domain of polyurea as "Network A", while the Maxwell element associated with the effect of the hard domain is referred to as "Network B".

3.2. Homogenization

The macroscopic deformation gradient $\mathbf{F}_{tot}$ is decomposed into a volumetric part $\mathbf{F}_{vol}$,

$$\mathbf{F}_{vol} = J^{1/3}\mathbf{1} \quad \text{with} \quad J = \det \mathbf{F}_{tot} \tag{2}$$

and an isochoric part $\mathbf{F}$

$$\mathbf{F} = J^{-1/3}\mathbf{F}_{tot}. \tag{3}$$

The constitutive model for the stresses induced by isochoric deformation is developed with the Taylor assumption in mind, i.e. the isochoric deformation gradients within both networks, $\mathbf{F}_{\mathrm{A}}$ and $\mathbf{F}_{\mathrm{B}}$, equal the macroscopic isochoric deformation gradient,

$$\mathbf{F} = \mathbf{F}_{\mathrm{A}} = \mathbf{F}_{\mathrm{B}}, \tag{4}$$

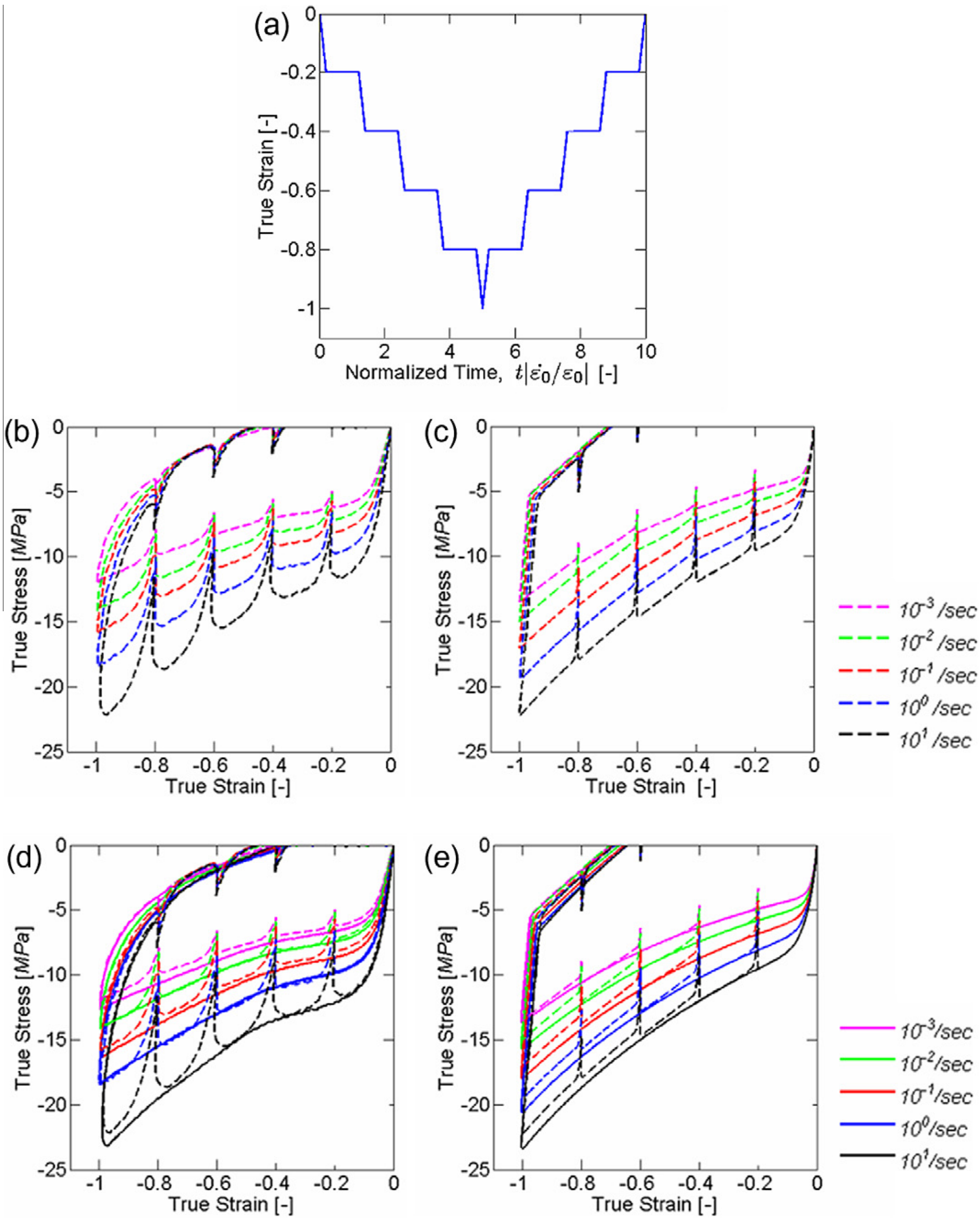

Fig. 3. Results for multistep loading/unloading. (a) History of applied strain. Note that time in the *x*-axis is normalized by the total testing duration $|\varepsilon_0/\dot{\varepsilon}_0|$ where $\varepsilon_0 = 1$ and $\dot{\varepsilon}_0 = 10^{-3},\ 10^{-2},\ 10^{-1},\ 10^{0}$ and 10^{1}/s. (b) Stress–strain curves from experiments and (c) corresponding simulations. (d) Comparison of results from continuous (solid lines) and multistep (dotted lines) loading/unloading experiments and (e) corresponding simulations.

In the context of micromechanism-inspired polymer models, the role of the microstructure is typically neglected. Instead, the constitutive equations for the individual phases predict a weighted macroscopic Cauchy stress (in the present case the weighted deviator stresses $\mathbf{T}_A$ and $\mathbf{T}_B$) such that the macroscopic stress deviator can be written as

$$\mathrm{dev}(\mathbf{T}) = \mathbf{T}_A + \mathbf{T}_B. \tag{5}$$

3.3. Constitutive equations for volumetric deformation

The volume change of polyurea under mechanical loading is very small as compared to the magnitude of isochoric deformation. For simplicity, we assume a nonlinear elastic relationship between the logarithmic volumetric strain and the hydrostatic part of the macroscopic Cauchy stress tensor,

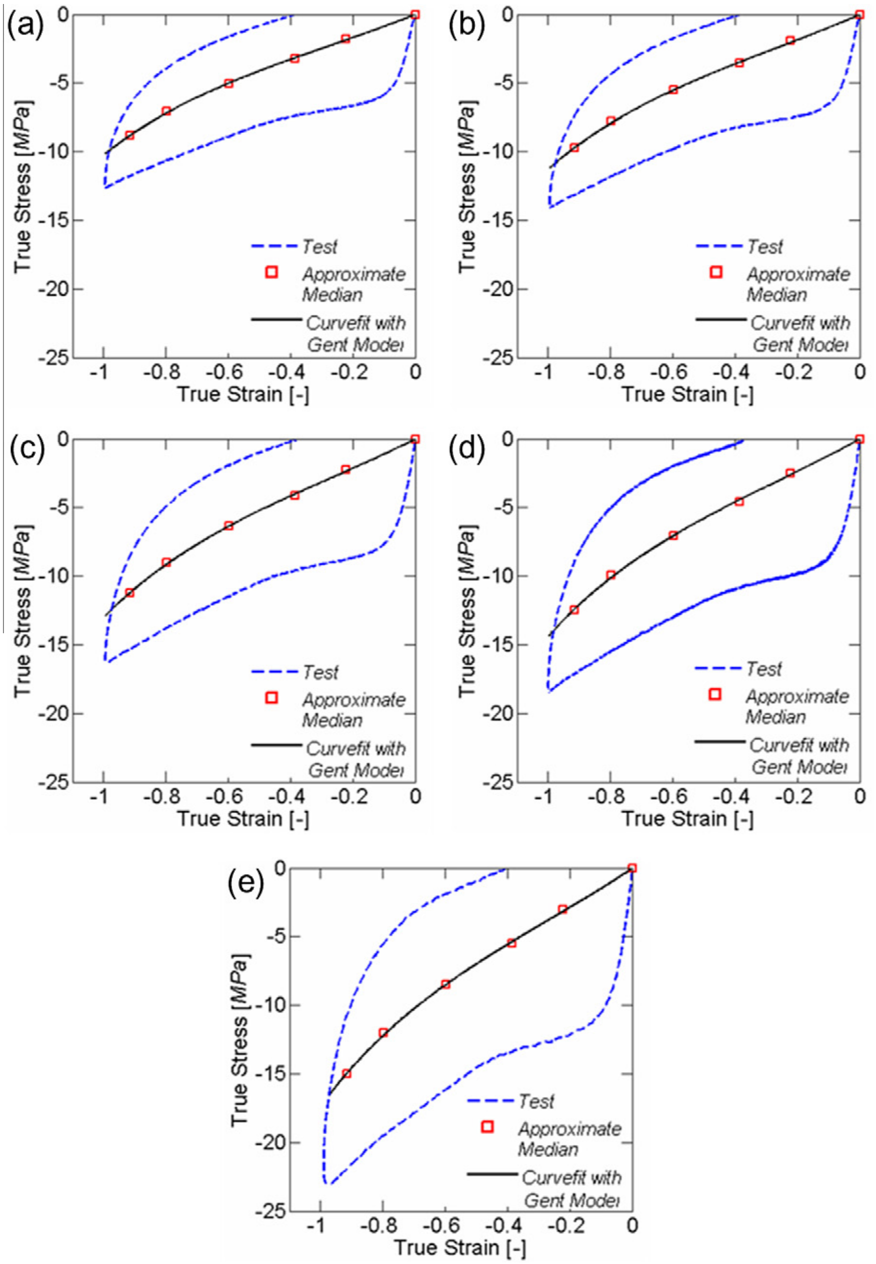

Fig. 4. Estimation of the behavior of Network A using the equilibrium path concept for different strain rates: (a) $\dot{\varepsilon} = 10^{-3}$/s, (b) $\dot{\varepsilon} = 10^{-2}$/s, (c) $\dot{\varepsilon} = 10^{-1}$/s, (d) $\dot{\varepsilon} = 10^{0}$/s, (e) $\dot{\varepsilon} = 10^{1}$/s.

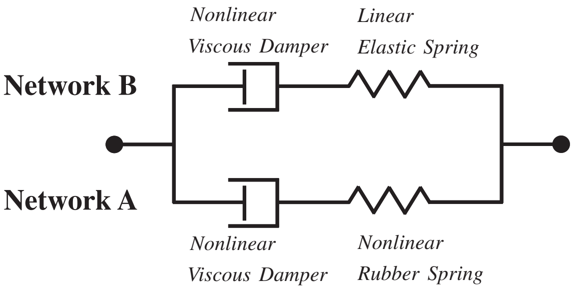

Fig. 5. Proposed rheological model for polyurea composed of two Maxwell elements in parallel.

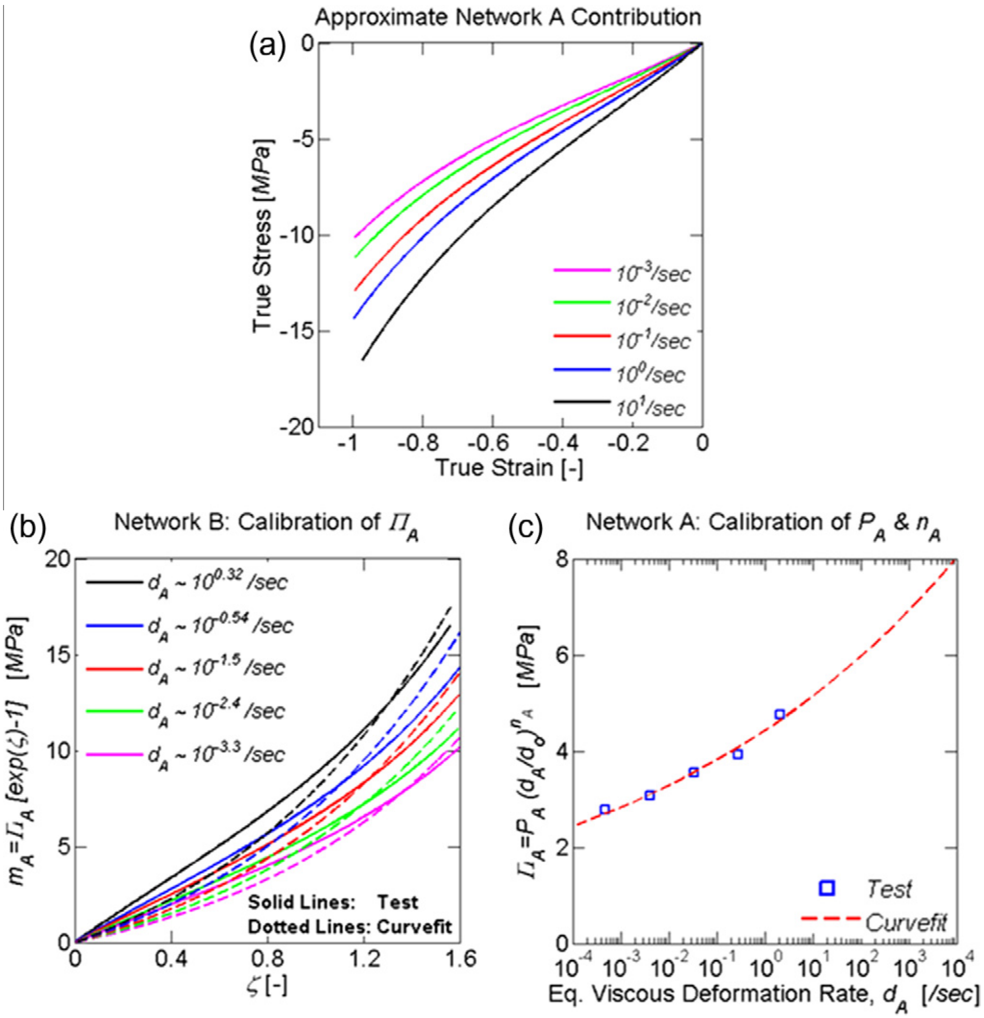

Fig. 6. Material model parameter identification for Network A. (a) Estimated experimental stress–strain curve for Network A; (b) equivalent Mandel stress as a function of the scalar deformation measure ζ ; (c) Π_A as function of the equivalent viscous deformation rate $\bar{d}_A$; identification of the model parameters P_A and n_A through power-law fit.

$$\frac{\mathrm{tr}(\mathbf{T})}{3} = \kappa \frac{\ln J}{J}, \tag{6}$$

where κ denotes the bulk modulus.

3.4. Maxwell model for isochoric deformation

The responses of Network A and Network B are described through Maxwell models. In this subsection, we provide the general framework for the formulation of the constitutive equations for Maxwell models. In the Sections 3.5 and 3.6, we will then specialize our equations for the individual networks.

3.4.1. Kinematics

Consider a Maxwell element K subject to an isochoric deformation gradient $\mathbf{F}_K$ with $\det \mathbf{F}_K = 1$. In the context of finite strain, we assume that the total isochoric deformation gradient can be multiplicatively decomposed into an elastic part $\mathbf{F}_K^e$ and a viscous part $\mathbf{F}_K^v$,

$$\mathbf{F}_K = \mathbf{F}_K^e \mathbf{F}_K^v. \tag{7}$$

Furthermore, we introduce the total, elastic and viscous rate of isochoric deformation tensors

$$\dot{\mathbf{F}}_K = \mathbf{L}_K \mathbf{F}_K, \quad \dot{\mathbf{F}}_K^e = \mathbf{L}_K^e \mathbf{F}_K^e \quad \text{and} \quad \dot{\mathbf{F}}_K^v = \mathbf{L}_K^v \mathbf{F}_K^v \tag{8}$$

with the relationship

$$\mathbf{L}_K = \mathbf{L}_K^e + \mathbf{F}_K^e \mathbf{L}_K^v \mathbf{F}_K^{e-1}. \tag{9}$$

Without loss of generality (see discussion by Gurtin and Anand (2005)), it is assumed that the viscous spin is zero for the deformation of the Maxwell elements. Formally, we write

$$\mathbf{D}_K^v := \mathbf{L}_K^v = \mathbf{L}_K^{vT}. \tag{10}$$

The rate of deformation tensor $\mathbf{D}_K^e$ may also be expressed as,

$$\mathbf{D}_K^e = \frac{1}{2} \mathbf{F}_K^{e-T} \dot{\mathbf{C}}_K^e \mathbf{F}_K^{e-1}. \tag{11}$$

In addition to the tensor description of the kinematics, we make use of the scalar deformation measure

$$\zeta = \sqrt{\mathrm{tr}(\mathbf{C}) - 3} \tag{12}$$

in our model formulation, where $\mathbf{C} = \mathbf{F}^T\mathbf{F}$ is the right Cauchy–Green tensor. The strain-like variable ζ is zero in the undeformed configuration and always positive for deformed configurations.

3.4.2. Thermodynamics and hyperelasticity

For isothermal conditions, the second law of thermodynamics for each Maxwell element reads

$$J\mathbf{T}_K : \mathbf{L}_K - \dot{\psi}_K \geqslant 0 \tag{13}$$

with the deviatoric Cauchy stress $\mathbf{T}_K$ and the free energy ψ_K (per unit initial volume). We impose the assumption of Green elasticity through the hyperelastic relationship (e.g. Ogden, 1997)

$$\mathbf{T}_K = \frac{2}{J} \mathrm{dev}\left\{ \mathbf{F}_K^e \frac{\partial \psi_K}{\partial \mathbf{C}_K^e} \mathbf{F}_K^{eT} \right\}, \tag{14}$$

where $\mathbf{C}_K^e = \mathbf{F}_K^{eT}\mathbf{F}_K^e$ denotes the right Cauchy–Green tensor of isochoric elastic deformation. Recall that we assume isochoric elastic deformation which implies $\det \mathbf{F}_K^e = 1$ and $\mathrm{tr}(\mathbf{D}_K^e) = 0$. Thus, it follows from (14) that

$$J\mathbf{T}_K : \mathbf{D}_K^e - \dot{\psi}_K = 0. \tag{15}$$

Using (9), (14), and (15) in (13) yields the thermodynamic constraint

$$J\mathbf{T}_K : \mathbf{F}_K^e \mathbf{L}_K^v \mathbf{F}_K^{e-1} = J\mathbf{F}_K^{eT} \mathbf{T}_K \mathbf{F}_K^{e-T} : \mathbf{D}_K^v \geqslant 0. \tag{16}$$

In the following, the Mandel stress

$$\mathbf{M}_K := J\mathrm{dev}\left\{ \mathbf{F}_K^{eT} \mathbf{T}_K \mathbf{F}_K^{e-T} \right\} \tag{17}$$

is used as the driving stress of viscous deformation while the viscoplastic constitutive equations are written such that

$$\mathbf{M}_K : \mathbf{D}_K^v \geqslant 0. \tag{18}$$

3.4.3. Flow rule for viscous flow

The direction of viscous flow is supposed to be aligned with the direction of the driving Mandel stress. Formally, we write the flow rule

$$\mathbf{M}_K = \eta_K \mathbf{D}_K^v \tag{19}$$

with the deformation and rate dependent viscosity $\eta_K \geqslant 0$. The rate dependent viscosity is defined through the nonlinear relationship $\bar{m}_K = \bar{m}_K(\bar{d}_K)$ between the equivalent Mandel stress

$$\bar{m}_K = \sqrt{\frac{3}{2} \mathbf{M}_K : \mathbf{M}_K} \tag{20}$$

and the equivalent viscous strain rate

$$\bar{d}_K = \sqrt{\frac{2}{3} \mathbf{D}_K^v : \mathbf{D}_K^v}. \tag{21}$$

Using (20) and (21) in (19), we obtain

$$\eta_K = \frac{2}{3} \frac{\bar{m}_K}{\bar{d}_K}. \tag{22}$$

3.5. Specialization of the Maxwell model for Network A

Network A represents the rubbery response of the soft domain which is modeled through a Maxwell element composed of a nonlinear elastic Gent spring and a nonlinear viscous damper.

3.5.1. Gent elasticity of Network A

For isochoric deformation, Gent's (1996) free energy function may be written as

$$\psi_{\mathrm{A}} = -\frac{1}{2}\mu_{\mathrm{A}} J_{\mathrm{A}} \ln\left(1 - \frac{\mathrm{tr}(\mathbf{C}^e_{\mathrm{A}}) - 3}{J_{\mathrm{A}}}\right) \tag{23}$$

with the material parameters $\mu_{\mathrm{A}} > 0$ (initial modulus) and $J_{\mathrm{A}} > 1$ (locking stretch). With this form of free energy, the Cauchy stress $\mathbf{T}_{\mathrm{A}}$ in Network A reads:

$$\mathbf{T}_{\mathrm{A}} = \frac{\mu_{\mathrm{A}}}{J}\left(1 - \frac{\mathrm{tr}(\mathbf{C}^e_{\mathrm{A}}) - 3}{J_{\mathrm{A}}}\right)^{-1} \mathrm{dev}\left(\mathbf{F}^e_{\mathrm{A}}\mathbf{F}^{eT}_{\mathrm{A}}\right). \tag{24}$$

3.5.2. Nonlinear viscous response of Network A

Fig. 6a suggests that the viscoelastic contribution to the stress of Network A increases monotonically as the deformation increases. Furthermore, the experimental results suggest a power-law relation between the viscosity η_{A} and the equivalent rate of viscous deformation. Thus, the nonlinear viscous evolution law for Network A is written as

$$\bar{m}_{\mathrm{A}} = \frac{3}{2}\eta_{\mathrm{A}}\bar{d}_{\mathrm{A}} = P_{\mathrm{A}}[\exp\zeta - 1]\left(\frac{\bar{d}_{\mathrm{A}}}{d_0}\right)^{n_{\mathrm{A}}} \tag{25}$$

with the reference rate of deformation $d_0 = 1/\mathrm{s}$, the viscosity constant $P_{\mathrm{A}} > 0$, and the exponent $n_{\mathrm{A}} > 0$ controlling the rate-sensitivity.

3.6. Specialization of the constitutive equations for Network B

3.6.1. Hencky elasticity of Network B

The stiffness of Network B governs the stiff macroscopic response of polyurea at small strains. Here, we make use of the isochoric part of Hencky's strain energy function,

$$\psi_{\mathrm{B}} = \mu_{\mathrm{B}}(\ln\mathbf{U}^e_{\mathrm{B}}) : (\ln\mathbf{U}^e_{\mathrm{B}}), \tag{26}$$

where the elastic stretch tensor $\mathbf{U}^e_{\mathrm{B}}$ is found from the polar decomposition of the elastic deformation gradient, $\mathbf{F}^e_{\mathrm{B}} = \mathbf{R}^e_{\mathrm{B}}\mathbf{U}^e_{\mathrm{B}}$ with $\mathbf{R}^{eT}_{\mathrm{B}}\mathbf{R}^e_{\mathrm{B}} = \mathbf{1}$ Upon evaluation, we obtain the deviatoric part of the Cauchy stress acting on Network B,

$$\mathbf{T}_{\mathrm{B}} = \frac{2\mu_{\mathrm{B}}}{J}\mathbf{R}^e_{\mathrm{B}}(\ln\mathbf{U}^e_{\mathrm{B}})\mathbf{R}^{eT}_{\mathrm{B}}. \tag{27}$$

The reader is referred to Anand and Ames (2006) or Gurtin et al. (2010) for details on the derivation of (27) from (26).

3.6.2. Nonlinear viscous response of Network B

Fig. 7a suggests that the overall viscoelastic response of Network B is similar to the linear viscoelastic response of a Maxwell model composed of a linear spring (of Young's modulus E) and a linear viscous damper (of viscosity η). The stress–strain (σ–ε) response of a Maxwell model with the linear components at a constant strain rate reads (e.g. Brinson and Brinson, 2008)

$$\sigma = E\tau\dot{\varepsilon}_0\left[1 - \exp\left(-\frac{\varepsilon}{\tau\dot{\varepsilon}_0}\right)\right], \tag{28}$$

where $\tau = \eta/E$ is the relaxation time, and $\dot{\varepsilon}_0$ is the applied constant strain rate. Note that even though the Maxwell model is composed of only linear elements, the stress–strain response is nonlinear at constant strain rates. However, our experiments suggest that the stress–strain response of Network B is linear for small strains regardless of strain rate.

Inspired by the results for the one-dimensional Maxwell model with linear components (Eq. (28)), we propose a constitutive equation that guarantees a linear elastic response of Network B at small strains,

$$\bar{m}_{\mathrm{B}} = \sqrt{3}\mu_{\mathrm{B}}Q_{\mathrm{B}}\left(\frac{\bar{d}_{\mathrm{B}}}{d_0}\right)^{n_{\mathrm{B}}}\left\{1 - \exp\left[-\frac{\zeta}{Q_{\mathrm{B}}}\left(\frac{\bar{d}_{\mathrm{B}}}{d_0}\right)^{-n_{\mathrm{B}}}\right]\right\}, \tag{29}$$

where the dimensionless material constants Q_{B} and n_{B} characterize the viscous properties of Network B.

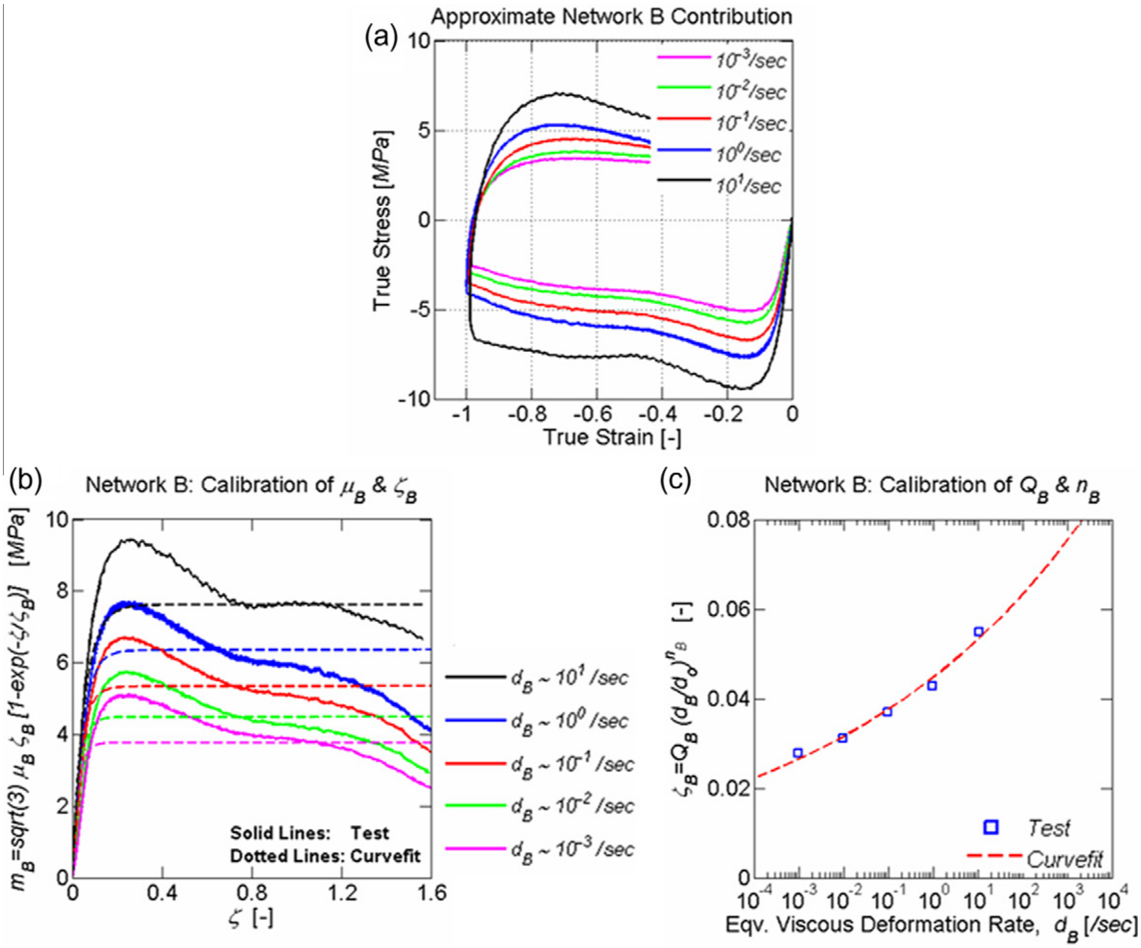

Fig. 7. Material model parameter identification for Network B. (a) Estimated experimental stress–strain curve for Network B; (b) equivalent Mandel stress as a function of the scalar deformation measure ζ; (c) ζ_B as function of the equivalent viscous deformation rate $\bar{d}_B$; identification of the model parameters Q_B and n_B.

4. Identification of the model parameters

The proposed constitutive model comprises eight material parameters: four parameters (μ_A, J_A, P_A, n_A) for Network A, three parameters (μ_B, Q_B, n_B) for Network B, and one parameter (κ) describing the elastic volumetric response. The constitutive equations are detailed for uniaxial stress loading in order to identify all material parameters from the monotonic loading and unloading compression experiments.

4.1. Constitutive equations for uniaxial loading

Under uniaxial stress loading, the macroscopic stress tensor takes the form

$$\mathbf{T} = \sigma \mathbf{e}_1 \otimes \mathbf{e}_1, \tag{30}$$

where σ is the true stress (macroscopic Cauchy stress) while the macroscopic deformation gradient reads

$$\mathbf{F}_{tot} = \lambda_1 \mathbf{e}_1 \otimes \mathbf{e}_1 + \lambda_2 [\mathbf{e}_2 \otimes \mathbf{e}_2 + \mathbf{e}_3 \otimes \mathbf{e}_3], \tag{31}$$

$$J = \det \mathbf{F}_{tot} = \lambda_1 (\lambda_2)^2. \tag{32}$$

At the network level, the isochoric part of the deformation gradient may be expressed as a function of the stretch λ,

$$\mathbf{F} = \lambda \mathbf{e}_1 \otimes \mathbf{e}_1 + \frac{1}{\sqrt{\lambda}} [\mathbf{e}_2 \otimes \mathbf{e}_2 + \mathbf{e}_3 \otimes \mathbf{e}_3] \quad \text{with} \quad \lambda = \left(\frac{\lambda_1}{\lambda_2}\right)^{\frac{2}{3}}. \tag{33}$$

The total stretch of a Maxwell element K can be decomposed further into its elastic part λ_K^e and the viscous part λ_K^v,

$$\lambda = \lambda_K^e \lambda_K^v. \tag{34}$$

Using this notation, the kinematic variables used in our constitutive equations may be expressed as a function of the elastic and viscous stretches and their respective time derivatives:

$$\operatorname{tr}\mathbf{C}_K^e = (\lambda_K^e)^2 + \frac{2}{\lambda_K^e}, \tag{35}$$

$$\operatorname{dev}\left(\mathbf{F}_K^e\mathbf{F}_K^{eT}\right) = \frac{2}{3}\left((\lambda_K^e)^2 - \frac{1}{\lambda_K^e}\right)\left(\mathbf{e}_1\otimes\mathbf{e}_1 - \frac{1}{2}\mathbf{e}_2\otimes\mathbf{e}_2 - \frac{1}{2}\mathbf{e}_3\otimes\mathbf{e}_3\right), \tag{36}$$

$$\ln\mathbf{U}_K^e = \ln(\lambda_K^e)\left(\mathbf{e}_1\otimes\mathbf{e}_1 - \frac{1}{2}\mathbf{e}_2\otimes\mathbf{e}_2 - \frac{1}{2}\mathbf{e}_3\otimes\mathbf{e}_3\right), \tag{37}$$

$$\zeta = \sqrt{\lambda^2 + \frac{2}{\lambda} - 3}, \tag{38}$$

$$\bar{d}_K = \frac{|\dot{\lambda}_K^v|}{\lambda_K^v}. \tag{39}$$

The deviatoric stress tensors $\mathbf{T}_K$ acting on the Maxwell elements are written as

$$\mathbf{T}_K = \frac{\sigma_K}{3}(2\mathbf{e}_1\otimes\mathbf{e}_1 - \mathbf{e}_2\otimes\mathbf{e}_2 - \mathbf{e}_3\otimes\mathbf{e}_3), \tag{40}$$

while

$$\sigma = \sigma_\mathrm{A} + \sigma_\mathrm{B}. \tag{41}$$

σ_A and σ_B are true stresses acting on Network A and B, respectively. Using expressions (30)–(41), we obtain the simplified constitutive equations for uniaxial loading:

(1) Volumetric deformation induced nonlinear elasticity with the model parameter κ,

$$\sigma = 3\kappa\frac{\ln J}{J}. \tag{42}$$

(2) Gent elasticity of Network A with the model parameters J_A and μ_A,

$$\sigma_\mathrm{A} = \frac{\mu_\mathrm{A}}{J}\frac{(\lambda_\mathrm{A}^e)^2 - \frac{1}{\lambda_\mathrm{A}^e}}{1 - \frac{1}{J_\mathrm{A}}\left((\lambda_\mathrm{A}^e)^2 + \frac{2}{\lambda_\mathrm{A}^e} - 1\right)}. \tag{43}$$

(3) Nonlinear viscous response of Network A with the model parameters P_A and n_A,

$$|\sigma_\mathrm{A}| = \frac{P_\mathrm{A}}{J}(\exp\zeta - 1)\left(\frac{\bar{d}_\mathrm{A}}{d_0}\right)^{n_\mathrm{A}}. \tag{44}$$

(4) Hencky elasticity of Network B with the model parameter μ_B,

$$\sigma_\mathrm{B} = \frac{3\mu_\mathrm{B}}{J}\ln(\lambda_\mathrm{B}^e). \tag{45}$$

(5) Nonlinear viscous response of Network B with the model parameters Q_B and n_B,

$$|\sigma_\mathrm{B}| = \sqrt{3}\frac{\mu_\mathrm{B}}{J}Q_\mathrm{B}\left(\frac{\bar{d}_\mathrm{B}}{d_0}\right)^{n_\mathrm{B}}\left\{1 - \exp\left[-\frac{\zeta}{Q_\mathrm{B}}\left(\frac{\bar{d}_\mathrm{B}}{d_0}\right)^{-n_\mathrm{B}}\right]\right\}. \tag{46}$$

4.2. Model calibration

The 1-D calibration process is composed of two steps: the parameters $\mu_\mathrm{A}, J_\mathrm{A}, P_\mathrm{A}, n_\mathrm{A}, \mu_\mathrm{B}, Q_\mathrm{B}$ and n_B are identified assuming material incompressibility ($J = 1$), before the bulk modulus κ is estimated based on the Lamé moduli and the Poison's ratio. A summary of all identified material parameters is given in Table 1.

4.2.1. Material parameters of Network A (μ_A, J_A, P_A, n_A)

The model is calibrated such that the response of Network A describes the rate dependency of the average stress–strain curves in the continuous compression experiments. As discussed in Section 3.1 (see also Fig. 6a), the stress $\sigma_\mathrm{A} = \sigma_\mathrm{A}(\lambda, \bar{d}_\mathrm{A})$ for a given strain rate amplitude $\bar{d}_\mathrm{A}$ is approximated by the average of the measured loading and unloading stress–strain curves at a total strain rate $\dot{\varepsilon}$,

$$\sigma_\mathrm{A}(\lambda, \bar{d}_\mathrm{A}) \cong \frac{1}{2}[\sigma(\lambda, \dot{\varepsilon}) + \sigma(\lambda, -\dot{\varepsilon})] \quad \text{with} \quad \bar{d}_\mathrm{A} \cong |\dot{\varepsilon}|. \tag{47}$$

Table 1
Summary of material parameters indentified from monotonic loading/unloading tests under five different strain rates.

Isochoric part of Network A	Rubber spring	μ_A	7.00 MPa
		J_A	10.7
	Viscous damper	P_A	4.42 MPa
		n_A	0.0646
Isochoric part of Network B	Linear spring	μ_B	82.3 MPa
	Viscous damper	Q_B	0.0447
		n_B	0.0755
Volumetric part		κ	829 MPa

The material parameters (μ_A, J_A, P_A, n_A) for Network A are calibrated in an iterative manner:

1. Assuming $\lambda_A^e(t) \cong \lambda(t)$, we estimate (μ_A, J_A) from the best fit of (43) to the experimentally obtained stress–strain curve for the highest strain rate case (here: $|\dot{\varepsilon}| = 10^1/\text{s}$).
2. For the remaining strain rates, we calculate $\lambda_A^e(t)$ based on (43) using (μ_A, J_A).
3. Using the relationship $\lambda_A^v(t) = \lambda(t)/\lambda_A^e(t)$, we calculate $|\sigma_A|$ as a function of the strain-like variable ζ for each experiment (Fig. 6b); in Fig. 6b, the curve labels indicate the average effective viscous strain rate $\bar{d}_A$.
4. The parameters P_A and n_A are then obtained from the approximation (44) of the curves shown in Fig. 6c.
5. It is useful to evaluate the term $\Pi_A = |\sigma_A|/(\exp\zeta - 1)$ from each experimental curve. Π_A is a function of the effective viscous strain rate $\bar{d}_A$ only and independent of the total strain. In other words, each curve shown in Fig. 6b reduces to a single data point in Fig. 6c. The subsequent curve fit $\Pi_A = \frac{P_A}{J}\left(\frac{\bar{d}_A}{d_0}\right)^{n_A}$ of the data points in Fig. 6c yields the model parameters P_A and n_A.

After completing Steps 1–5, we obtain:

$$\begin{aligned} &\mu_A = 6.85\ \text{MPa}, \quad J_A = 11.0, \\ &P_A = 4.44\ \text{MPa}, \quad n_A = 0.0648. \end{aligned} \tag{48}$$

A second calibration loop is performed, starting with $\lambda_A^e(t) = \lambda(t)/\lambda_A^v(t)$ in Step 1, where $\lambda_A^v(t)$ is the viscous deformation predicted by the model parameters (48). Subsequent evaluation yields:

$$\begin{aligned} &\mu_A = 7.00\ \text{MPa}, \quad J_A = 10.7, \\ &P_A = 4.42\ \text{MPa}, \quad n_A = 0.0646. \end{aligned} \tag{49}$$

The calibration procedure has been stopped at this point as additional iterations did not improve the accuracy of the curve fit.

4.2.2. Material parameters of Network B (μ_B, Q_B, n_B)

The stress contribution of Network B is obtained by subtracting the identified stress contribution of Network A (using the parameters (49) in (44)) from the original stress–strain curve for each strain rate,

$$\sigma_B(\lambda, \dot{\varepsilon}) = \sigma(\lambda, \dot{\varepsilon}) - \sigma_A(\lambda, \bar{d}_A), \tag{50}$$

where $\bar{d}_A$ corresponds to the average viscous strain rates that have been determined throughout the calibration of Network A. Fig. 7 shows the corresponding results for different strain rates. According the proposed rheological model, viscoelastic behavior of Network B should be symmetric with respect to the stress, i.e. $\sigma_B(\lambda, -\dot{\varepsilon}) = -\sigma_B(\lambda, \dot{\varepsilon})$. However, the curves in Fig. 7 illustrate that this symmetry assumption holds only approximately true when using the calibrated analytical expression (44) for Network A. In close analogy with the calibration procedure for Network A, we identify the model parameters associated with Network B:

1. We assume $\lambda_B^e(t) \cong \lambda(t)$ for the highest strain rate case (i.e. strain rate of 10^1/s), and
2. determine μ_B from the best curve fit for the experimental stress–strain curve for the loading phase using (45).
3. Using μ_B, we can then calculate $\lambda_B^e(t)$ and $\lambda_B^v(t) = \lambda(t)/\lambda_B^e(t)$ for the other experiments. The corresponding $|\sigma_B|$ versus ζ curves are shown in Fig. 7b. According to (47), we have

$$|\sigma_B| = \sqrt{3}\frac{\mu_B}{J}\zeta_B\left[1 - \exp\left(-\frac{\zeta}{\zeta_B}\right)\right], \tag{51}$$

where $\zeta_B = Q_B\left(\frac{\bar{d}_B}{d_0}\right)^{n_B}$ is a function of the strain rate only. Thus, we determine ζ_B from the approximation of (51) to the $|\sigma_B|$ vs. ζ curves. Subsequently, the material constants Q_B and n_B are found from plotting ζ_B as a function of the effective viscous strain rate $\bar{d}_B$.

A second parameter identification loop is performed using $\lambda_B^e(t) = \lambda(t)/\lambda_B^v(t)$ leading to:

$$\begin{aligned} &\mu_B = 82.3\ \text{MPa}, \\ &Q_B = 0.0447, \quad n_B = 0.0755. \end{aligned} \tag{52}$$

4.2.3. Bulk modulus of material (κ)

The initial shear modulus for the proposed model is the sum of the shear modulus of each network, i.e., $\mu = \mu_A + \mu_B = 89.3$ MPa. Experiments revealed that the Poisson's ratio of $v = 0.45$ is nearly rate-independent throughout the deformation up to the strain of 100% (Shim and Mohr, 2009). Since the free energy for the volumetric deformation is based on the elastic model in (6), we can determine the bulk modulus using the relation between the elastic moduli,

$$\kappa = \frac{2\mu(1+v)}{3(1-2v)} = 829\ \text{MPa}. \tag{53}$$

5. Comparison of simulation and experiments

The constitutive model has been programmed as a user material subroutine for the finite element software Abaqus/explicit. Using the identified material model parameters, we perform the simulations of all experiments described in Section 2.

5.1. Continuous compression

Fig. 2c summarizes the numerically predicted stress–strain curves for different strain rates. Similarly to the experiments (Fig. 2b), the simulation results exhibit a high strain rate sensitivity during the loading phases. In addition, the characteristic convergence of the stress–stain curves for different loading velocities is also captured by the simulations. The comparisons of experiment and simulation for individual strain rates are shown in Fig. 8a–e. The stress–strain curves show a better agreement during loading than during unloading. The loading portions typically feature the largest error for small strains (less than 0.2) while good predictions are achieved for large strains. The predicted response during unloading is too stiff for all strain rates, i.e. the simulations reach a stress of zero at larger compressive strains than measured in the experiments. From an energetic point of view, it is worth noting that the differences during the loading phase underestimate the mechanical work, while the work is overestimated during unloading. However, these two errors compensate each other when calculating the viscous energy dissipation for the entire loading–unloading cycle. In other words, despite small errors in the stress level during loading and unloading, the overall energy dissipation is well predicted over a wide range of strain rates.

The graphs in Fig. 8 also depict the predicted individual contributions of Network A (dotted blue[1] line) and Network B (dashed green line). During the model calibration, we assumed that the effective viscous strain rate $\bar{d}_A$ is the same during loading and unloading, which implies that Network A exhibits the same stress–strain response during loading and unloading. However, since the total viscous strain λ_A^v keeps on decreasing during unloading (the driving stress for Network A is compression during both loading and unloading) even though λ increases, the decrease of the stress level is faster during unloading than the corresponding increase during loading (hysteresis behavior of a Maxwell element). The differences between the loading and unloading portion for Network A (blue dashed curves) illustrate this behavior.

The model's symmetric response of Network B (the green dashed curves show only the loading portion) is characterized by a plateau over a wide range of strains. Since the elastic strains in Network B are small, the driving stress of viscous deformation in Network B changes rapidly from compression during loading to tension during unloading. As a result, the effective rate of viscous deformation $\bar{d}_B$ is the same during loading and unloading which is consistent with the assumptions made during calibration. Thus, it is concluded that the differences between the experiments and model predictions are associated with the response of Network A.

5.2. Multistep compression

Fig. 3c provides an overview on the simulation results for all loading cases next to the experimentally-measured stress–strain curves from multistep compression tests. A direct comparison of the experimental and the simulation results for each loading velocity is shown in Fig. 9a–e. Overall, we observe the same model accuracy as for the monotonic loading and unloading experiments, i.e. the model slightly underestimates the stress level for small strains and predicts a faster decrease in stress level after reversal of the loading direction.

The relaxation behavior of Network B is symmetric for loading and unloading (green dashed lines in Fig. 9). Conversely, the stress–strain curves for Network A (blue dotted lines in Fig. 9) reveal that stress relaxation is more pronounced during the loading phase, while unloading is mainly elastic. This non-symmetric feature of Network A is also visible at the

---

[1] For interpretation of color in Figs. 1, 8 and 9, the reader is referred to the web version of this article.

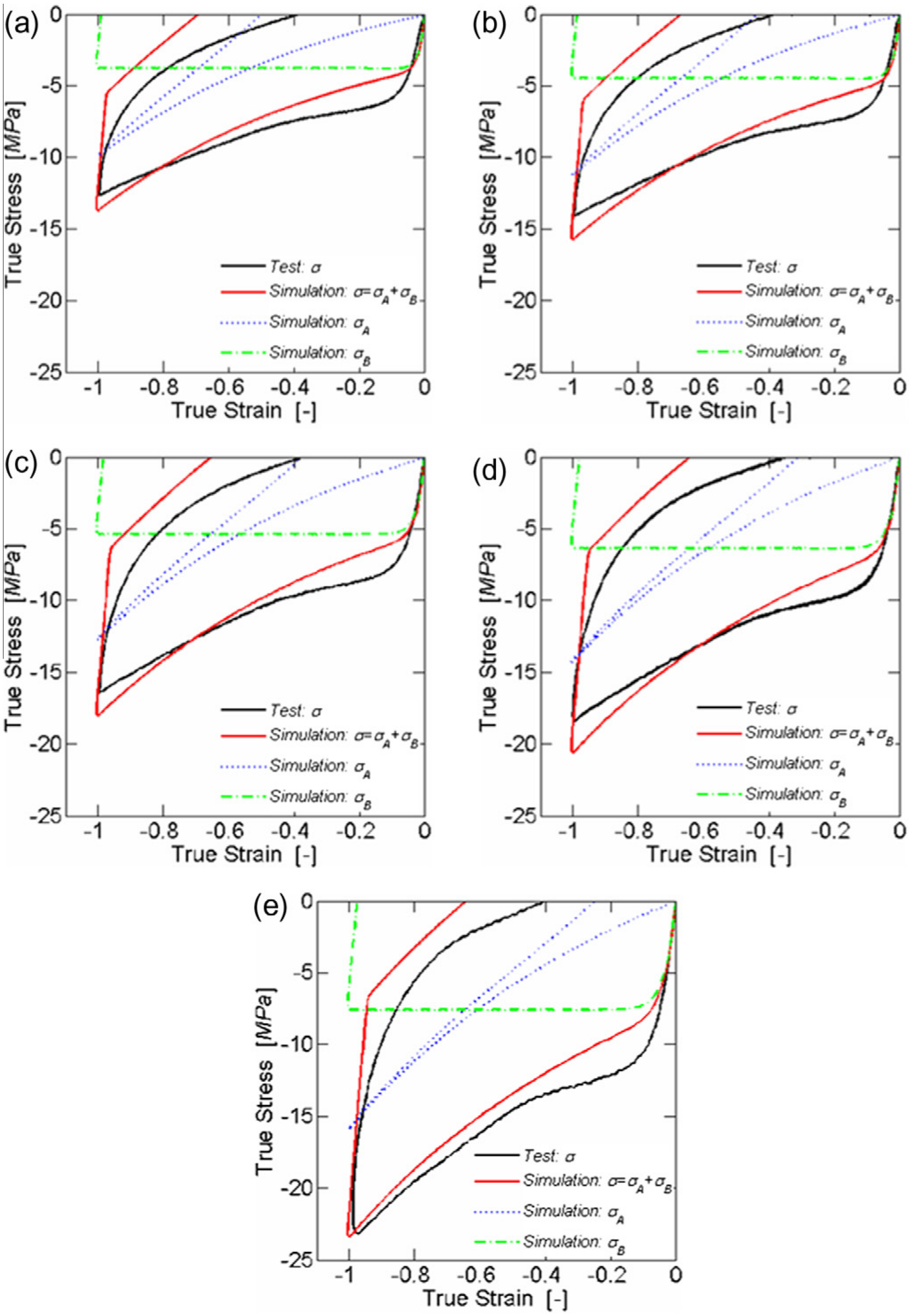

Fig. 8. Comparison of simulation results and experiments for continuous loading–unloading cycles. (a) $\dot{\varepsilon} = 10^{-3}$/s, (b) $\dot{\varepsilon} = 10^{-2}$/s, (c) $\dot{\varepsilon} = 10^{-1}$/s, (d) $\dot{\varepsilon} = 10^{0}$/s and (e) $\dot{\varepsilon} = 10^{1}$/s.

macroscopic level where the model predicts the experimental observation of a faster relaxation during loading than during unloading. The model provides accurate estimates of the relaxation-induced stress decrease (jump) for small strains during the loading phase, while this decrease is underestimated at large strains. This is attributed to the fact that the stress contribution of Network B reaches its plateau level at small strains; as a result, the amplitude of stress relaxation within Network B is very similar for small and large strains.

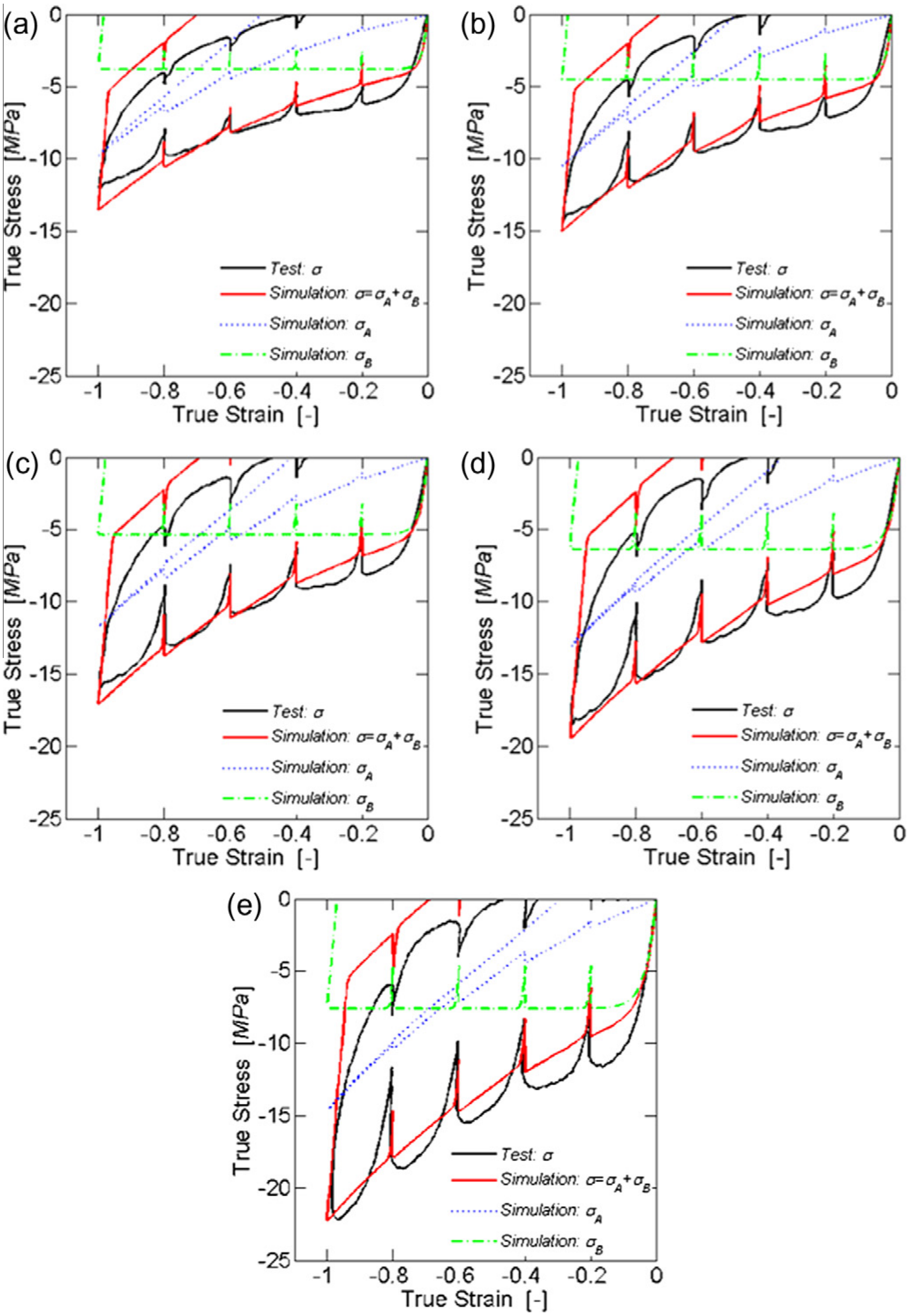

Fig. 9. Comparison of simulation results and experiments for multistep loading–unloading cycles. (a) $\dot{\varepsilon} = 10^{-3}/\mathrm{s}$, (b) $\dot{\varepsilon} = 10^{-2}/\mathrm{s}$, (c) $\dot{\varepsilon} = 10^{-1}/\mathrm{s}$, (d) $\dot{\varepsilon} = 10^{0}/\mathrm{s}$ and (e) $\dot{\varepsilon} = 10^{1}/\mathrm{s}$.

5.3. Relaxation

Fig. 1b shows the predicted stress histories for all relaxation experiments. In addition, the histories of the relaxation modulus are presented in Fig. 1d. The relaxation modulus histories are well predicted for the entire range of strains. However, the comparison of the true stress versus time curves indicates that the model predicts slower stress relaxation than observed in the experiments. Similar conclusions may be drawn from the comparison of the experimental and simulated isochronous stress–strain curves. Observe that the instantaneous stress–strain curves agree well with the test results, while the long-term behavior (e.g. blue curves for 616 s) predicted by the model overestimates the stress level at large strains.

5.4. Discussion

The model is able to predict the strain rate dependent loading and relaxation behavior polyurea with reasonable accuracy. Furthermore, the model provides good estimates of the rate dependent viscous dissipation throughout the loading–unloading cycles. In the present rheological framework of two parallel Maxwell elements, the identification of the behavior of Network A is important. Here, the response of Network A has been defined through the rate-dependent average stress–strain response; the mechanical response of Network A is identical throughout compressive loading and compressive unloading. Furthermore, in the particular case of polyurea, the rate dependent average stress–strain response depends on the absolute value of the total true strain rate. The response of the calibrated constitutive model illustrates that the assumption of a Maxwell model does not lead to an exact description of the material behavior for both loading and unloading. The hysteresis behavior for loading and unloading at a constant total strain rate is an inherent feature of Maxwell models. Consequently, the rate dependency of the average stress–strain response (which is hysteresis free) cannot be represented accurately by a Maxwell model. An attempt has been made to calibrate the material model parameters using a numerical parameter identification scheme (minimization of the error between the experiments and simulations). In other words, the separation of the contributions of Network A and Network B has been omitted throughout the material model parameters identification. However, the identified model response was not more satisfactory as improvements on the unloading response could only be obtained at the expense of the quality of the loading curve prediction.

It is noted that the model by Boyce et al. (2000) can also describe the monotonic loading part of the present experiments. However, after calibrating the model by Boyce et al. (2000), we observed a poor agreement with experimental data for unloading. Recall that the proposed model can successfully capture the characteristic convergence of the unloading behavior for different strain rates. Furthermore, the Boyce et al. (2000) model describes the viscous behavior as a thermally activated process, while the proposed model includes a phenomenological viscous formulation which requires less material model parameters.

In order to come up with an improved constitutive model, one may consider a different rheological model for Network A, but to the best of the authors' knowledge, no thermodynamically consistent model has been published in the open literature that can model the apparent elastic (same loading and unloading curve), but yet strain rate dependent behavior of Network A. Thus, alternative modeling approaches need to be explored in the future. One thermodynamically consistent option is the introduction of loading and unloading conditions for viscous evolution. However, more research is needed at the microstructural (i.e. molecular) level to justify such loading and unloading conditions from a mechanism point of view.

6. Conclusions

The large strain compression response of polyurea is investigated for strain rates ranging from 10^{-3}/s to 10^{1}/s. Continuous and multistep loading and unloading experiments are performed in addition to simple relaxation tests. The experimental results reveal that the so-called equilibrium path concept breaks down in the case of polyurea. In contradiction with the definition of the equilibrium path, the identified average stress–strain curves in continuous loading–unloading experiments depend on the rate of loading. Thus, as an alternative to the equilibrium path concept based rheological models of the Zener type, a new constitutive model is formulated assuming two parallel Maxwell elements. The finite strain constitutive equations are outlined in detail. Subsequently, the eight material model constants are calibrated to describe the mechanical behavior of polyurea. The model predictions are in good agreement with the experimental results. The characteristic convergence of the unloading paths for different strain rates is successfully captured by the model. Furthermore, the rate dependent viscous dissipation throughout a loading–unloading cycle is described with reasonable accuracy. The predicted unloading behavior is too stiff which is associated with the limitations of the Maxwell model that describes the soft domain of polyurea.

Acknowledgements

Thanks are due to Professor Tomasz Wierzbicki from MIT for valuable discussion. The partial financial support through Office of Naval Research (ONR) Grant #N00014-07-1-0821 and the French National Center for Scientific Research (CNRS) is gratefully acknowledged.

References

Ames, N.M., Srivastava, V., Chester, S.A., Anand, L., 2009. A thermo-mechanically coupled theory for large deformations of amorphous polymers. Part II: Applications. International Journal of Plasticity 25, 1495–1539.

Amin, A.F.M.S., Alam, M.S., Okui, Y., 2002. An improved hyperelasticity relation in modeling viscoelasticity response of natural and high damping rubbers in compression: experiments, parameter identification and numerical verification. Mechanics of Materials 34, 75–95.

Amin, A.F.M.S., Lion, A., Sekita, S., Okui, Y., 2006. Nonlinear dependence of viscosity in modeling the rate-dependent response of natural and high damping rubbers in compression and shear: experimental identification and numerical verification. International Journal of Plasticity 22, 1610–1657.

Amirkhizi, A.V., Isaacs, J., McGee, J., Nemat-Nasser, S., 2006. An experimentally-based viscoelastic constitutive model for polyurea, including pressure and temperature effects. Philosophical Magazine 86, 5847–5866.

Anand, L., Ames, N.M., 2006. On modeling the micro-indentation response of an amorphous polymer. International Journal of Plasticity 22, 1123–1170.

Anand, L., Ames, N.M., Srivastava, V., Chester, S.A., 2009. A thermo-mechanically coupled theory for large deformations of amorphous polymers. Part I: Formulation. International Journal of Plasticity 25, 1474–1494.

Areias, P., Matous, K., 2008. Finite element formulation for modeling nonlinear viscoelastic elastomers. Computational Methods in Applied Mechanical Engineering 197, 4702–4717.

Arruda, E.M., Boyce, M.C., 1993. A 3-dimensional constitutive model for the large stretch behavior of rubber elastic materials. Journal of the Mechanics and Physics of Solids 41, 389–412.

Ayoub, C., Zaïri, F., Naït-Abdelaziz, M., Gloaguen, J.M., 2010. Modelling large deformation behaviour under loading–unloading of semicrystalline polymers: application to a high density polyethylene. International Journal of Plasticity 26, 329–347.

Bergström, J.S., Boyce, M.C., 1998. Constitutive modeling of the large strain time-dependent behavior of elastomers. Journal of the Mechanics and Physics of Solids 46, 931–954.

Bergström, J.S., Hilbert, L.B., 2005. A constitutive model of predicting the large deformation thermomechanical behavior of fluoropolymers. Mechanics of Materials 37, 899–913.

Bernstein, B., Kersley, E.A., Zapas, L.J., 1963. A study of stress relaxation with finite strain. Transaction of the Society of Rheology 7, 391–410.

Bogoslovov, R.B., Roland, C.M., 2007. Viscoelastic effects on the free retraction of rubber. Journal of Applied Physics 102, 063531.

Boyce, M.C., Socrate, S., Llana, P.G., 2000. Constitutive model for the finite deformation stress–strain behavior of poly(ethylene terephthalate) above the glass transition. Polymer 41, 2183–2201.

Brinson, H.F., Brinson, L.C., 2008. Polymer Engineering Science and Viscoelasticity: An Introduction. Springer Science + Business Media, LLC, New York, NY. p. 327.

Colak, O.U., 2005. Modeling deformation behavior of polymers with viscoplasticity theory based on overstress. International Journal of Plasticity 21, 145–160.

Coleman, B.D., Noll, W., 1961. Foundations of linear viscosity. Reviews of Modern Physics 33, 239–249.

Dupaix, R.B., Boyce, M.C., 2007. Constitutive modeling of the finite strain behavior of amorphous polymers in and above the glass transition. Mechanics of Materials 39, 39–52.

Dusunceli, N., Colak, O.U., 2008. Modelling effects of degree of crystallinity on mechanical behavior of semicrystalline polymers. International Journal of Plasticity 24, 1224–1242.

Fragiadakisa, D., Gamacheb, R., Bogoslovova, R.B., Roland, C.M., 2010. Segmental dynamics of polyurea: effect of stoichiometry. Polymer 51, 178–184.

Gent, A.N., 1996. A new constitutive relation for rubber. Rubber Chemistry and Technology 69, 59–61.

Gurtin, M.E., Anand, L., 2005. The decomposition F = F^eF^p, material symmetry, and plastic irrotationality for solids that are isotropic-viscoplastic or amorphous. International Journal of Plasticity 21, 1686–1719.

Gurtin, M.E., Fried, E., Anand, L., 2010. The Mechanics and Thermodynamics of Continua. Cambridge University Press, New York, NY. p. 293.

Haupt, P., Lion, A., 2002. On finite linear viscoelasticity of incompressible isotropic materials. Acta Mechanica 159, 87–124.

Hoo Fatt, M.S., Ouyang, X., 2007. Integral-based constitutive equation for rubber at high strain rates. International Journal of Solids and Structures 44, 6491–6506.

Hoo Fatt, M.S., Ouyang, X., 2008. Three-dimensional constitutive equations for styrene butadiene rubber at high strain rates. Mechanics of Materials 40, 1–16.

Huber, N., Tsakmakis, C., 2000. Finite deformation viscoelasticity laws. Mechanics of Materials 32, 1–18.

Johlitz, M., Steeb, H., Diebels, S., Chatzouridou, A., Batal, J., Possart, W., 2007. Experimental and theoretical investigation of nonlinear viscoelastic polyurethane systems. Journal of Materials Science 42, 9894–9904.

Johnson, A.R., Quigley, C.J., Mead, J.L., 1994. Large-strain viscoelastic constitutive models for rubber, I. Formulations. Rubber Chemistry and Technology 67, 904–917.

Johnson, A.R., Quigley, C.J., Freese, C.E., 1995. A viscohyperelastic finite element model for rubber. Computational Methods in Applied Mechanical Engineering 127, 163–180.

Khan, A.S., Farrokh, B., 2006. Thermo-mechanical response of nylon 101 under uniaxial and multi-axial loadings: Part I, Experimental results over wide ranges of temperatures and strain rates. International Journal of Plasticity 22, 1506–1529.

Khan, A., Zhang, H., 2001. Finite deformation of a polymer: experiments and modeling. International Journal of Plasticity 17, 1167–1188.

Khan, A.S., Lopez-Pamies, O., Kazmi, R., 2006. Thermo-mechanical large deformation response and constitutive modeling of viscoelastic polymers over a wide range of strain rates and temperatures. International Journal of Plasticity 22, 581–601.

Krempl, E., McMahon, J.J., Yao, D., 1984. Viscoplasticity based on overstress with a differential growth law for the equilibrium stress. Mechanics of Materials 5, 35–48.

Kröner, E., 1960. Allgemeine kontinuumstheorie der versetzungen und eigenspannungen. Archive for Rational Mechanics and Analysis 4, 273–334.

Le Tallec, P., Rahier, C., Kaiss, A., 1993. Three-dimensional incompressible viscoelasticity in large strains: formulation and numerical approximation. Computer Methods in Applied Mechanics and Engineering 109, 233–258.

Lee, E.H., 1969. Elastic plastic deformation at finite strain. ASME Journal of Applied Mechanics 36, 1–6.

Leonov, A.I., 1976. Nonequilibrium thermodynamics and rheology of viscoelastic polymer media. Rheologica Acta 15, 85–98.

Lianis, G., 1963. Constitutive equations of viscoelastic solids under large deformations. A & ES Report No. 63-5, Purdue University.

Lion, A., 1996. A constitutive model for carbon black filled rubber: experimental investigations and mathematical representation. Continuum Mechanics and Thermodynamics 8, 153–169.

Lion, A., 1997a. A physically based method to represent the thermo-mechanical behaviour of elastomers. Acta Mechanica 123, 1–25.

Lion, A., 1997b. On the large deformation behaviour of reinforced rubber at different temperatures. Journal of the Mechanics of Physics of Solids 45, 1805–1834.

Lockett, F.J., 1972. Nonlinear Viscoelastic Solids. Academic Press Inc., New York, NY. p. 59.

Lubliner, J., 1985. A model of rubber viscoelasticity. Mechanics Research Communications 12, 93–99.

McGuirt, C.W., Lianis, G., 1970. Constitutive equations for viscoelastic solids under finite uniaxial and biaxial deformations. Transaction of the Society of Rheology 14, 117–134.

Mulliken, A.D., Boyce, M.C., 2006. Mechanics of the rate-dependent elastic–plastic deformation of glassy polymers from low to high strain rates. International Journal of Solids and Structures 43, 1331–1356.

Ogden, R.W., 1997. Non-linear Elastic Deformations. Dover Publications, Mineola, NY.

Palm, G., Dupaix, R.B., Castro, J., 2006. Large strain mechanical behavior of poly(methyl methacrylate) (PMMA) near the glass transition temperature. Journal of Engineering Materials and Technology 128, 559–563.

Qi, H.J., Boyce, M.C., 2005. Stress–strain behavior of thermoplastic polyurethanes. Mechanics of Materials 37, 817–839.

Quintavalla, S.J., Johnson, S.H., 2004. Extension of the Bergstrom–Boyce model to high strain rates. Rubber Chemistry and Technology 77, 972–981.

Reese, S., Govindjee, S., 1998. A theory of finite viscoelasticity and numerical aspects. International Journal of Solids and Structures 35, 3455–3482.

Roland, C.M., 1989. Network recovery from uniaxial extension I: elastic equilibrium. Rubber Chemistry Technology 62, 863–879.

Roland, C.M., Twigg, J.N., Vu, Y., Mott, P.H., 2007. High strain rate mechanical behavior of polyurea. Polymer 48, 574–578.

Samson, N., Mechin, F., Pascault, J., 1997. Relationships between synthesis and mechanical properties of new polyurea materials. Journal of Applied Polymer Science 65, 2265–2280.

Sarva, S.S., Deschanel, S., Boyce, M.C., Chen, W., 2007. Stress–strain behavior of a polyurea and a polyurethane from low to high strain rates. Polymer 48, 2208–2213.

Shim, J., Mohr, D., 2009. Using split Hopkinson pressure bars to perform large strain compression tests on polyurea. International Journal of Impact Engineering 36, 1116–1127.

Shim, V.P.W., Yang, L.M., Lim, C.T., Law, P.H., 2004. A visco-hyperelastic constitutive model to characterize both tensile and compressive behavior of rubber. Journal of Applied Polymer Science 92, 523–531.

Sidoroff, F., 1974. Un modèle viscoélastique non linéaire avec configuration intermédiaire. Journal de Mécanique 13, 679–713.

Tomita, Y., Azuma, K., Naito, M., 2008. Computational evaluation of strain-rate-dependent deformation behavior of rubber and carbon-black-filled rubber under monotonic and cyclic straining. International Journal of Mechanical Sciences 50, 856–868.

Yang, L.M., Shim, V.P.W., Lim, C.T., 2000. A visco-hyperelastic approach to modelling the constitutive behaviour of rubber. International Journal of Impact Engineering 24, 545–560.